

FIRST RESULTS FROM VIPER: DETECTION OF SMALL-SCALE ANISOTROPY AT 40 GHZ

J. B. PETERSON^{1,2}, G. S. GRIFFIN¹, M. G. NEWCOMB¹, D. L. ALVAREZ¹, C. M. CANTALUPO¹, D. MORGAN¹, K. W. MILLER³, K. GANGA⁴, D. PERNIC⁵, M. THOMA⁵

Draft version February 1, 2008

ABSTRACT

Results of a search for small-scale anisotropy in the cosmic microwave background (CMB) are presented. Observations were made at the South Pole using the Viper telescope, with a $.26^\circ$ (FWHM) beam and a passband centered at 40 GHz. Anisotropy band-power measurements in bands centered at $\ell = 108, 173, 237, 263, 422$ and 589 are reported. Statistically significant anisotropy is detected in all bands.

Subject headings: cosmology: cosmic microwave background, observation

1. INTRODUCTION

Most theories of the early universe predict the presence of a peak in the cosmic microwave background (CMB) anisotropy power spectrum (White, Scott, and Silk 1994). In cold dark matter models the position of this peak, the first acoustic peak, is $\ell \sim 220\Omega_{total}^{\frac{1}{2}}$ where $\Omega_{total} = \Omega_{matter} + \Omega_\lambda$ is determined by the total matter/energy density in the universe (Kamionkowski, Spergel, and Sugiyama 1994). In many inflation models Ω_{total} is forced to one; these inflation models make the specific prediction that the power spectrum will peak at $\ell \sim 220$.

CMB anisotropy data have recently been analyzed in comparison to theoretical models (Lineweaver and Barbosa 1998, Ratra, et al. 1999, Hu 1999, Scott 1999) and there is evidence for a peak in the power spectrum. That conclusion has in the past been based on combined analysis of many different experiments at various angular scales, since most previous individual experiments did not cover the range of ℓ best suited to search for the expected peak. The Viper telescope, when used at 40 GHz, has a 0.26° beam (FWHM) which sweeps 3.6° across the sky. Thus Viper has sensitivity from $\ell \sim 100$ to $\ell \sim 600$, spanning the range of interest for tests of inflation and other cosmological models.

2. INSTRUMENT

The optics of the Viper telescope consist of four mirrors arranged in an off-axis configuration. The 2.15m primary mirror, together with the secondary mirror, form an aplanatic gregorian. Radiation from a distant object, converging to a focus after reflection from the primary and secondary, is reflected again by a flat, electrically driven chopping mirror, and then directed into the photometer feed horns using a fast hyperbolic condensing mirror. The chopping mirror is placed at an exit pupil of the gregorian, i.e. at an image of the primary formed by the sec-

ondary. This means that tilting the chopping mirror is nearly equivalent, optically, to tilting the primary.

Because the optical design has a clear aperture, the secondary and condensing mirrors can be built oversized without the blockage that would occur in an on-axis telescope. We have done this to improve optical efficiency and reduce pickup of earth emission. The primary mirror has incoherent extension panels that increase the effective diameter to 3 m, and the entire telescope is housed in a 10 meter diameter conical reflecting baffle to further reduce pickup of earth emission. Details of the instrument design are available at the Viper web page⁶.

For the observations reported here, the photometer used on Viper was a two pixel receiver based on HEMT (high electron mobility transistor) amplifiers cooled to 10-20 K temperature. The amplifiers are coupled to the telescope through corrugated feed horns chosen to provide a half-power illumination pattern on the primary of about 1 m diameter. This photometer, called Corona, measures the total power from 38 to 44 GHz, in two sub-bands.

The instrument is calibrated using ambient temperature and liquid-nitrogen-immersed calibrators, temporarily inserted so they fill the illumination pattern of the feed horns. The efficiency of the optics, $90 \pm 5\%$, is measured by tracing the beam through the telescope using ambient-temperature absorbers, and is checked by measuring the brightness temperature of the Moon. The total calibration uncertainty is 8 %.

3. OBSERVATIONS

The chopping mirror oscillates at a frequency of 2.35 Hz, causing the beam to sweep back and forth across the sky in the co-elevation direction at nearly constant velocity. Using observations of Venus (figure 1), we find that the chopper throw is $3.60 \pm .01^\circ$, and the beam is $.26 \pm .01^\circ$ wide (FWHM) with a Gaussian shape and no noticeable eccentricity. This is consistent with similar measurements

¹Department of Physics, Carnegie Mellon University, Pittsburgh, PA 15213

²email:jbp@cmu.edu

³JILA and Department of Physics, University of Colorado, Boulder, CO 80303

⁴IPAC, Caltech, Pasadena CA 91125 and PCC, Collège de France, F-75231 Paris Cedex 5, France

⁵Yerkes Observatory, Williams Bay, WI 53191

⁶<http://cmbr.phys.cmu.edu/viper>

made using Centaurus A and a remote Gunn oscillator.

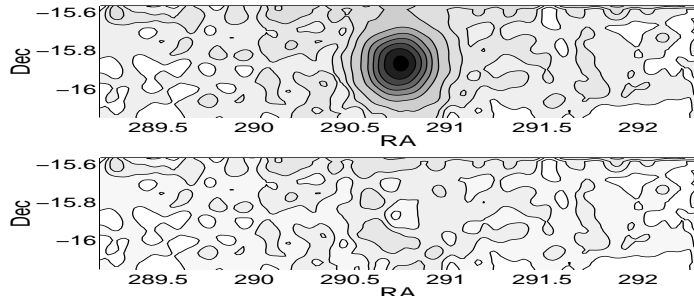


FIG. 1.— Antenna Beam Pattern. The top image is the beam pattern of the Viper/Corona system measured using Venus as a source. The image is created by sweeping the beam in co-elevation using the chopping mirror while stepping through many elevation angles. We model our beam pattern as a 0.26° FWHM Gaussian. The bottom panel shows the fit residual after the model beam pattern has been subtracted from the data in the top panel. Contours are at 25, 50, 100, 200...700 mK.

For the observations discussed here, the telescope slews at a constant declination, -52.03° (epoch 2000.0), between 11 overlapping fields spaced $.77^\circ$ apart. It dwells at each field for 13.7 s, and spends 5.0 seconds slewing to the next field. For fields $i = 1\dots11$, the movement pattern is: $i=1,3,5,7,9,11,10,8,6,4,2$. In this manner, a single *scan* containing 151 s of data is completed in 206 s. A total of 135 hours of data, recorded in June 1998, are included in this analysis.

Interspersed with these observations, the Carina nebula was swept for a few minutes every 2 hours as a pointing check. Over the period of this data set, the measurements of the nebula center varied by < 1 arcminute (rms). We take this to be our relative pointing precision.

To determine the absolute pointing accuracy of the instrument, we scanned 6 bright (≥ 25 mK) objects at declinations $-63.0 \leq \delta \leq -47.5$ in the galactic plane. We use a simple 5-parameter pointing model⁷ to align these objects with their radio coordinates, determined using the Parks-MIT-NRAO (PMN) 4.8 GHz survey (Griffith and Wright 1993, Wright, et al. 1994). We find a pointing residual of 2.4 arcminutes rms. Using this pointing model, we scan 30 Doradus ($5h38m43s - 69^\circ06'03''$) and find it 3.8 arcminutes from its PMN coordinates. This is the largest discrepancy between the radio positions and the positions we find at 40 GHz, so we believe our absolute pointing to be accurate to within 4 arcminutes in the region $-69.1 \leq \delta \leq -47.5$.

4. SYNCHRONOUS OFFSET SUBTRACTION

As the chopping mirror moves, sweeping the beam across the sky, the photometer uses different areas of the telescope mirrors. The illumination of the primary mirror hardly changes as the chopping mirror moves, but the illumination pattern on the secondary changes substantially. The emissivity of the secondary might vary across its surface if, for example, emissive snow had accumulated in an uneven pattern. In addition, scattering by snow grains on the optics might vary as the chopper sweeps. These effects produce what are called synchronous offsets, which appear

at the detector output to be variations of sky brightness but are in fact instrumental in origin. If these offsets come from the telescope they will produce the same apparent sky structure regardless of where the telescope is pointed so they can be identified and removed. The removal process is described in the next section.

5. DATA REDUCTION

If any sample deviates by more than 5-sigma from the average, the sweep containing that sample is deleted. This serves to remove electrical interference that appears in a few places in the data. If more than 2 sweeps are deleted from any scan, the entire scan is deleted.

We then determine the synchronous offset. For each scan, we co-add over all the sweeps in each field to produce a single waveform. We then co-add all 11 fields to produce an average chopper-synchronous offset waveform for the scan. This offset waveform, typically less than 4 mK rms in size, is subtracted from the waveform for each field.

Finally we look for rapid changes in the synchronous offset. The offset might change if snow is falling on the telescope mirrors, or if clouds are moving through the scan. We co-add the first and last 5 fields in each scan. When these two waveforms are subtracted, the standard deviation of the residual indicates the rate of change of the offset over the period of a scan. If this exceeds 2.5 mK rms the scan is deleted. This removes a total of 42 hours of data.

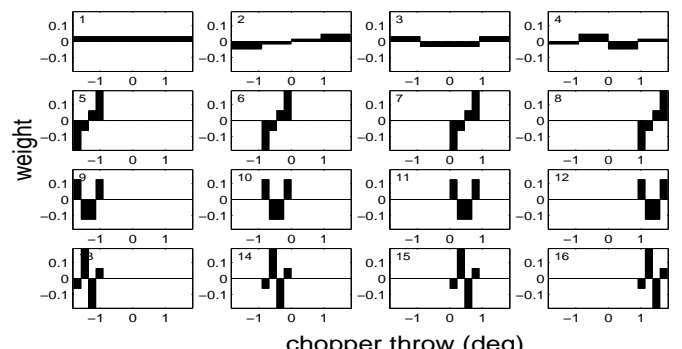


FIG. 2.— Modulation Weighting Functions. The sixteen modulation weighting functions used in this analysis are shown versus position within the 3.60° sweep. Some patterns differ only by translation. There are seven unique patterns allowing measurement of the anisotropy power spectrum across six ranges of spatial frequency ℓ . The number in the top left of the upper panels is the index j .

6. MODULATIONS

By multiplying the waveform for each field by the weighting functions in figure 2 we synthesize 16 orthogonal beam patterns. The weighting functions w_{jk} are derived using the orthogonality and normalization conditions:

$$\sum_{k=1}^N w_{j_1 k} \cdot w_{j_2 k} = 0 \quad j_1 \neq j_2, 1 \leq j \leq N \quad (1)$$

$$\sum_{k=1}^N |w_{jk}| = 2 \quad (2)$$

⁷These parameters are: the offsets of the azimuth and elevation encoders, the distance of the two feed horns from the optical center, and the dewar angle in the focal plane.

Here j is an index identifying the function, and k indexes N positions across the sky. Because fluctuations of atmospheric emission (sky noise) typically have much larger spatial scales than the region of sky we sweep, the dominant contributions of the atmospheric emission to our measured signals appear as constant or gradient waveforms across the sweep.

To generate the w_{jk} , we start with a constant w_{1k} and a gradient w_{2k} . Each successive modulation w_{jk} is a described by a polynomial of order $j-1$. This constraint, along with equations (1) and (2), generates a unique set of functions that are similar to the Legendre Polynomials, except that they are defined over a discrete basis. For $j > 2$ these weighting functions offer excellent sky noise rejection because they are orthogonal to the constant and gradient waveforms.

In this analysis we have divided the sweeps into 4 segments, and each segment is weighted with $w_{1k} \dots w_{4k}$. We then divide each segment into 4 smaller bins, which are similarly weighted.

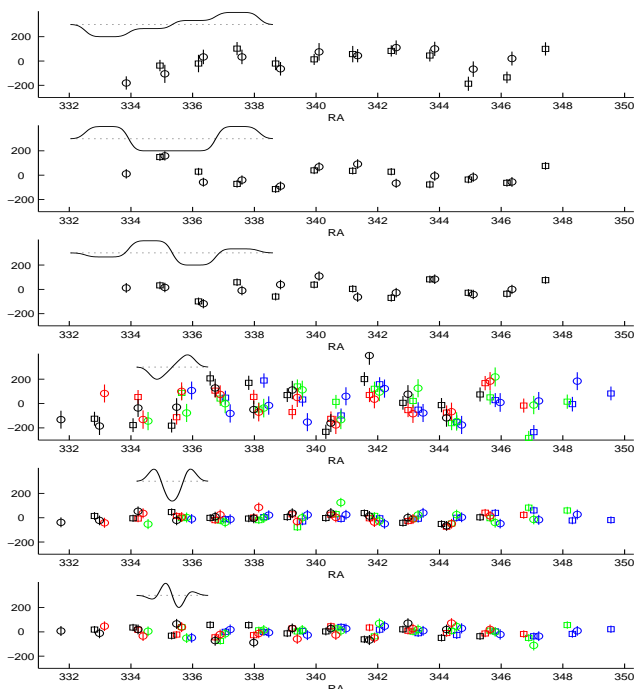


FIG. 3.— Temperature Structure on the Sky. Sky temperature structure is shown for six modulations. The modulation functions, smoothed with the antenna pattern, are shown in the upper left corner of each plot. Circles and squares indicate measurements taken with the left and right feed horns, respectively. For the last 3 modulations, the chopper throw is divided into 4 measurements each, denoted by a different colors. Referring to figure 3, modulations 5, 9 and 13 are black, modulations 6, 10 and 14 are red, modulations 7, 11 and 15 are green, and modulations 8, 12 and 16 are blue.

Some of the resulting 16 patterns are translated equivalents of others. There are seven unique patterns. The constant weighting provides no information on sky structure and is discarded. We had not expected to be able to detect sky structure with the gradient weighting w_{2k} , but we find that the South Pole winter atmosphere is so stable that statistically significant structure is in fact detected. We continue the analysis with the six remaining unique weighting functions. The beam patterns for the

six weightings are shown in figure 3 and the corresponding window functions are shown in figure 4.

7. BAND POWER ESTIMATES

The goal of our observations is to measure C_ℓ , the power spectrum of CMB anisotropy (see Hu, Sugiyama and Silk 1997, Hu 1999). For each modulation we determine the band-power (Bond et al. 1998), using the matrix method (Netterfield, et al. 1997). That is, we generate two matrices, a theory matrix and a noise matrix.

The theory matrix accounts for correlations of modulated sky temperature structure that would be expected in a noiseless observation of the sky. This matrix consists of correlations calculated between pairs of modulated observations on separated fields. The theory matrix is calculated without reference to the data from the sky, using lagged window functions. It accounts for the fact that our fields overlap and that pairs of temperature values for nearby locations are expected to be correlated.

In contrast to the theory matrix, the noise matrix is calculated from the set of measured temperatures of the sky (Lineweaver et al. 1994). There are a number of possible sources of correlated noise in these observations. For example, on days with patchy cloud cover we see variations of apparent sky brightness that are actually coming from the cloud pattern passing over the telescope (sky noise). This noise is likely to be correlated since individual clouds move from field to field. These correlations must be accounted for if the uncertainty of the observation is to be correctly estimated. The noise matrix accomplishes this since its elements are the cross-correlations of data sets recorded for each field.

To determine the range of band-power values that reasonably fit our data we carry out a likelihood test for each modulation, establishing a most likely C_ℓ value. We also estimate an uncertainty in C_ℓ by determining a confidence interval containing 67 % of the integrated likelihood. These values are plotted in figure 4. In estimating C_ℓ we used the method of Church, et al. 1998 to compensate for the effect of offset subtraction. The error bars in figure 4 do not include the calibration uncertainty.

8. FOREGROUNDS

Because these observations were made over a small range of observing frequency, we make use of observations made with other telescopes to constrain possible astronomical foregrounds.

The observations reported here lie within the region previously studied with Python (Coble, et al. 1999), a region which was carefully selected to have a very low level of foreground emission. Using Python the region has been mapped with $\sim 1^\circ$ angular resolution at 40 GHz and 90 GHz. These maps show strongly correlated sky structure. The sky structure detected with Python has a frequency spectrum consistent with the CMB and not consistent with the spectrum of any single known foreground source. Using data from the Infra-Red Astronomical Satellite (IRAS) (Beichman, et al. 1988) and using PMN data, the Python team has estimated that of the $\sim 80 \mu\text{K}$ RMS sky structure detected less than $\sim 1 \mu\text{K}$ rms is due to dust, synchrotron or free-free emission. Galactic structure has a spatial power spectrum that falls rapidly with ℓ , and the

Viper observations reported here cover a higher range of ℓ than the Python results. We therefore accept the Python foreground analysis as indicating that extended (Galactic) foregrounds make no significant contribution to the sky structure measured on these fields with Viper.

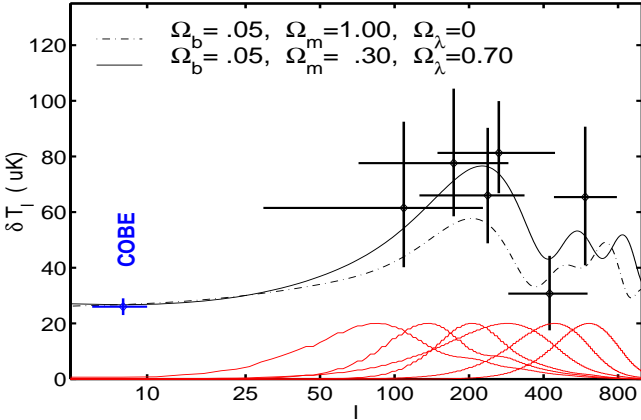


FIG. 4.— The Anisotropy Power Spectrum. The band-power for six modulations is shown as a function of the spatial frequency ℓ , along with two theoretical curves calculated using `cmbfast` (Seljak and Zaldarriaga 1996). Also shown is an average COBE band-power data point. At the bottom of the plot are window functions (scaled to the same height) for each modulation.

Viper has a beam about 1/16 the area of the Python beam so foregrounds due to extra-galactic point sources are a more significant concern. To estimate the contribution due to unresolved sources, we examined a total of 160 PMN 4.8 GHz sources that fall close to the region we observed. The brightest source in the vicinity of our observations is PMNJ2256-5158. This source can be expected to contribute substantially to the sky structure we detect because it has flux $700 \mu\text{Jy}$ at 4.8 GHz, our sweep passes directly over it, and its spectrum has been measured to fall only slowly between 2.8 and 4.8 GHz ($S_\nu \propto \nu^\beta; \beta(2.8..4.8) = -0.7$). We compared our data for the region near this source to that expected from 5158 and found a statistically significant match. If we treat our measured sky brightnesses in this region as due entirely to 5158 (i.e. ignoring any CMB structure), we can estimate a spectral index for this source by comparing our data to the 4.8 GHz PMN flux. We get $\beta(4.8..40) = -0.9 \pm 0.2$. Because this falls in line with the PMN spectral index, we elect to make a correction for this source, by extrapolating from 4.8 GHz, using spectral index -0.9 , and then removing the contribution to C_ℓ due to 5158. The correction is small: the greatest effect is in the high ℓ bands and amounts to about $2 \mu\text{K}$. All other PMN sources in the region are at least five times weaker and would require spectral index > 1.0 to contribute significantly. We make no correction for any other PMN source. The data presented in figure 3 include the emission of 5158 (i.e. we have

applied no correction to this data), but the C_ℓ spectrum in figure 4 has been corrected.

Data taken with IRAS at $100 \mu\text{m}$ (3000 GHz) show eight sources near the region observed. Extrapolating from 3000 GHz to 40 GHz, using a conservative emissivity law $\epsilon \propto \nu^1$, we find that none of the sources can contribute as much as $1 \mu\text{K}$. We make no correction for IRAS sources.

We can not rule out the possibility that an undetected population of extra-galactic objects contributes to fine scale sky structure at 40 GHz. Our study of possible extra-galactic foregrounds assumes that sources detected at lower frequencies have spectra that fall with frequency when compared to the CMB, as radio-bright galaxies do. We also assume that the objects detected at $100 \mu\text{m}$ with IRAS have spectra that rise with frequency over this frequency range. This is indeed the pattern seen in infrared-bright galaxies. There remains the possibility, however, that a class of previously undetected objects exists with spectra that closely mimic the CMB. As an example consider a dusty galaxy at redshift $z = 10$. At that epoch the CMB temperature was 30K so dust in such a galaxy might have been heated to just a few Kelvin above the CMB temperature. That dust emission, redshifted to millimeter wavelengths, would have a frequency spectrum peaking just above the CMB peak and would be exceedingly difficult to distinguish from CMB structure. While there is currently no evidence that any such objects did exist at redshift 10, it will take fine-beam millimeter wavelength sky survey data to rule out the contribution of such sources.

9. DISCUSSION

We interpret the sky structure we have detected as CMB anisotropy. The increase above COBE anisotropy levels, expected in flat inflation models to appear near $\ell \sim 220$, is evident in the data, as is a lower anisotropy level near the expected position of the first null at $\ell \sim 400$. Models with a significant cosmological constant appear to fit the data better than those with $\Lambda = 0$.

This work was supported by the National Science Foundation under cooperative agreement OPP-8920223 with the Center for Astrophysical Research in Antarctica and was also supported with internal CMU funds. We wish to thank Ted Griffith and Laszlo Varga for constructing and installing the Viper telescope. Mark Dragovan and Brian Crone did the initial optical design, and Hien Nguyen modified this design. We thank the following for contributions to Viper assembly and testing: Pamela Brann, Nicole Cook, Alex van Gaalen, Michael Vincent, Alex Japour, Mike Masterman and Mark Williams. We also thank the staff of the Amundsen-Scott research station at the South Pole.

REFERENCES

- Beichman, C.A., Neugebauer, G., Habing, H.J., Clegg, P.E. and Chester, T.J., IRAS Explanatory Supplement, Scientific and Technical Information Division National Aeronautics and Space Administration 1988 Washington, DC (1988).
- Bond, J. R., Jaffe, A. H. and Knox, L., Phys. Rev. D**57**, 2117 (1998), astro-ph 9708203.
- Church, S. E., Ganga, K. M., Ade, P. A. R., Holzapfel, W. L., Mauskopf, P. D., Wilbanks, T. M. and Lange, A. E., ApJ, **484**, 523 (1997). astro-ph 9702196
- Coble, K., Dragovan, M., Kovac, J., Halverson, N. W., Holzapfel, W. L., Knox, L., Dodelson, S., Ganga, K., Alvarez, D., Peterson, J. B., Griffin, G., Newcomb, M., Miller, K., Platt and S. R., Novak, G., ApJ, **519**, L5 (1999).

- Griffith, M. and Wright, A.E., *AJ*, **105**, 1666 (1993).
- Hu, W., Sugiyama, N. and Silk, J., *Nature*, **386**, 37 (1997), astro-ph/9604166.
- Hu, W., <http://www.sns.ias.edu/~whu/> (1999).
- Kamionkowski, M., Spergel, D. N., and Sugiyama, N., *ApJ*, **426**, L57 (1994), astro-ph/9401003.
- Lineweaver, C. H., Smoot, G. F., Bennett, C. L., Wright, E. L., Tenorio, L., Kogut, A., Keegstra, P. B., Hinshaw, G. and Banday, A. J., *ApJ*, **436**, 452 (1994).
- Lineweaver, C. H. and Barbosa, D. *ApJ*, **496**, 624 (1998).
- Netterfield, C. B., Devlin, M. J., Jarosik, N., Page, L. and Wollack, E. J., *ApJ*, **474**, 4766 (1997).
- Ratra, B., Stompor, R., Ganga, K., Rocha, C., Sugiyama, N. and Gorski, K., *ApJ*, **517**, 549 (1999)
- Scott, D., <http://www.astro.ubc.ca/people/scott/cmb.html> (1999).
- Seljak, U. and Zaldarriaga, M., *ApJ*, **469**, 437 (1996).
- White, M., Scott, D., and Silk, J., *ARA&A*, **32**, 319 (1994)
- Wright, A.E., Griffiths, M.R., Burke, B.F. and Ekers, R.D., *Astrophys. J., Suppl. Ser.*, **91**, 111 (1994)